RESEARCH ARTICLE

ADVANCED OPTICAL MATERIALS
www.advopticalmat.de

Two-Chromatic Printing Creates Skin-Inspired Geminate Patterns Featuring Crosstalk-Free Chemical and Physical Colors

Xiaojun Liu, Shuzhen Cui, Lang Qin, and Yanlei Yu**

Skin-inspired optical materials that combine both chemical and physical colors provide enhanced information capacity for potential applications in optical multiplexing and anti-counterfeiting technologies. However, the existing materials suffer from the limitations of an extremely narrow gamut and incompatibility with universal patterning methods to program dual-mode images. Here, novel two-chromatic printing technology is proposed to create full-color, high-resolution, and geminate patterns by newly designed fluorescent liquid crystal nanocomposites. Such nanocomposites consist of porous cholesteric liquid crystal networks embedded with core–shell CdSe/ZnS quantum dots to produce extended wide color palettes of both photoluminescence and Bragg reflection. The drop-on-demand two-chromatic printing technology simultaneously enables the construction and patterning of the nanocomposites in a high-precision way, orthogonally tuning the hues of two color palettes according to Grassmann's and Bragg's law. Therefore, the combination of different color generation mechanisms offers a versatile toolbox, which can be generalized to pigmentary, photonic, and even dynamic optical materials.

1. Introduction

The richest and most diverse color patterns in the animal kingdom appear on skins, which have evolved elegant combinations of pigmentary and structural elements to aid in optical functions for camouflage and signaling.[1–5] The secret behind the color patterns of the skin lies in the specialized dermal structures with two classes of cells, including chromatophores in the upper layer and iridophores in the lower layer (**Figure 1a**). The chromatophores contain pigmented granules to show chemical colors (e.g., pigmentary coloration and photoluminescence) and the iridophores comprise arranged translucent guanine proteins to exhibit physical colors (e.g., interference and Bragg reflection). Inspired by the skins, the researchers strive to design optical materials that produce both chemical and physical colors,[6–9] offering abundant optical states to increase the information capacity, including reflection wavelength, light polarization, fluorescent color, intensity, and lifetime value, for potential applications in optical multiplexing and anti-counterfeiting technologies.[10–13]

Fluorescent liquid crystals (LCs) recently have emerged as state-of-the-art optical materials with enhanced information capacity, because they inherit the luminescence properties of the embedded fluorophores (chemical color),[14–17] and, notably, demonstrate structural colors by manipulating the distribution and alignment of the LC molecules (physical color).[18–23] In light of the unique advantage of decoupled fluorescent and structural colors, geminate patterns that carry entirely distinct but crosstalk-free information have been created.[24–28] For example, holographic and fluorescent images have been integrated within the same volume of an LC polymer film containing a tetraphenylethene (TPE)-based derivative.[27] The periodic distribution of the polymer and LC are patterned by polymerization-induced phase separation to show the holographic images. The localized photocyclization of the TPE derivative reduces the emission intensity and thus facilitates the fluorescent images. Besides, reflective and fluorescent images have been simultaneously demonstrated by an array of cholesteric liquid crystal (CLC) microdroplets doped with a cyano-substituted oligo(p-phenylene vinylene) (cyano-OPV) derivative.[28] The 3D self-organized helical superstructures of the CLC microdroplets generate reflective images of structural colors, and programmable patterning of the microdroplets with or without the cyano-OPV derivative promises fluorescent images with high contrast.

However, the existing materials still face the great challenges of an extremely narrow gamut and incompatibility with universal patterning methods. On one hand, molecular self-organization or aggregation is an intrinsic nature of the LCs. To avoid the aggregation-caused quenching (ACQ) effect, fluorophores are limited to a minority of aggregation-induced emission (AIE) groups with a single hue of photoluminescence (cyan, yellow).[29–36] On the other hand, the LCs are a kind of fluid with a certain viscosity. Equally significant is the design of a coloration scheme to create geminate patterns with high

X. Liu, S. Cui, L. Qin, Y. Yu
Department of Materials Science & State Key Laboratory of Molecular Engineering of Polymers
Fudan University
Shanghai 200433, China
E-mail: qinlang@fudan.edu.cn; ylyu@fudan.edu.cn

The ORCID identification number(s) for the author(s) of this article can be found under https://doi.org/10.1002/adom.202302573

DOI: 10.1002/adom.202302573

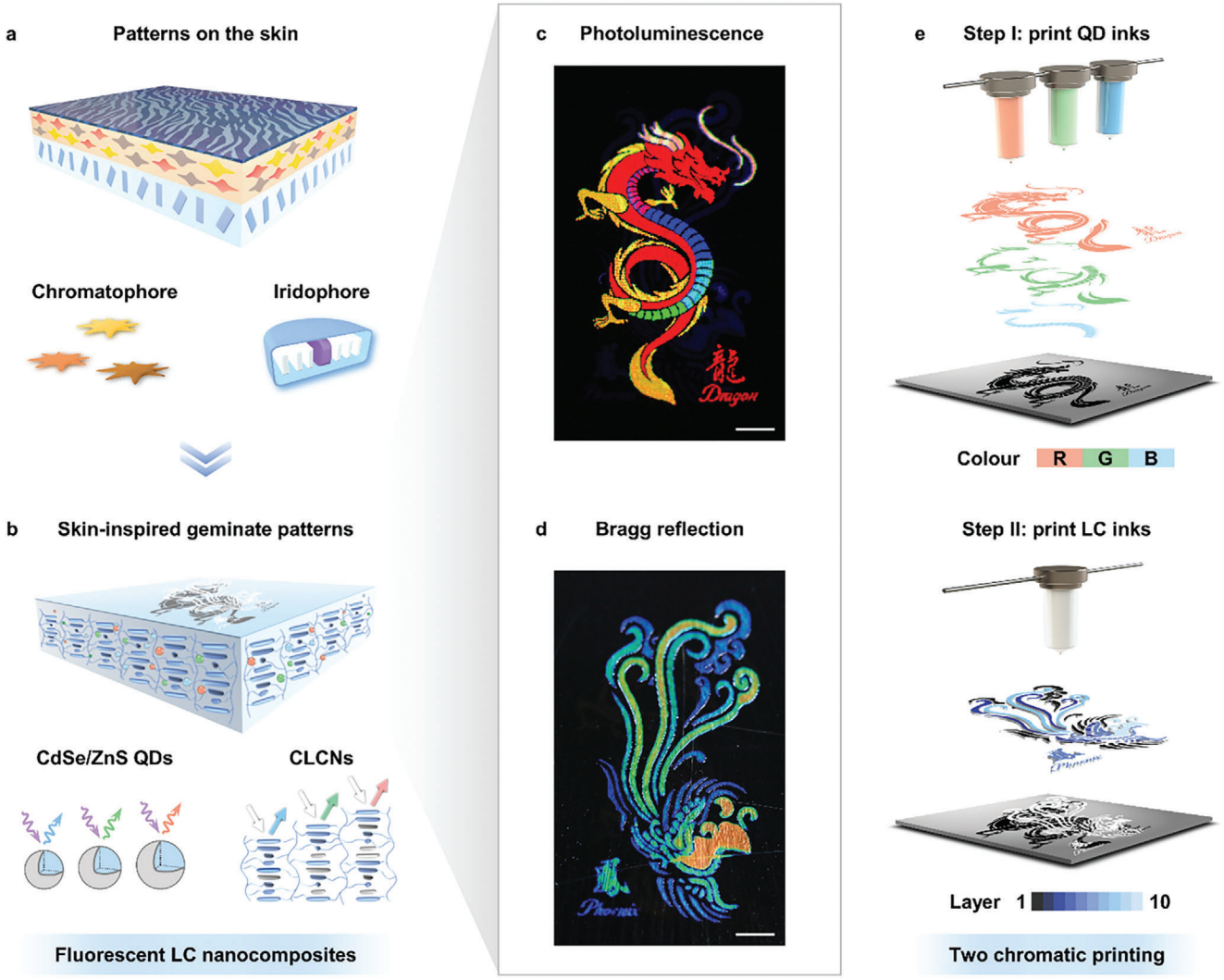

Figure 1. a) Schematic illustration to show the secret behind the patterns of the animal skins, where the coloration includes chemical color supplied by chromatophores and structural color determined by iridophore. b) Schematic illustration to show the skin-inspired geminate patterns of fluorescent liquid crystal (LC) nanocomposites composed of CdSe/ZnS quantum dots (QDs) and cholesteric LC networks (CLCNs). The QDs and CLCNs contribute to photoluminescence (chemical color) and Bragg reflection (structural color). c,d) Photographs of a full-color, high-resolution, and geminate pattern created by two-chromatic (2C) printing technology to show the images of fluorescent *Dragon* upon UV excitation c) and reflective *Phoenix* upon white light irradiation d). Scale bar, 5 mm. e) Schematic illustration to show the process workflow of 2C printing. The CLCNs are printed by the QD inks with red (R), green (G), and blue (B) fluorescent colors and the LC inks with different layers in sequence.

definition by locally regulating the LC alignment as well as the location of fluorophores.

Herein, we design novel fluorescent liquid crystal nanocomposites to create skin-inspired geminate patterns by two-chromatic (2C) printing technology (Video S1, Supporting Information). The nanocomposites-a new paradigm of the fluorescent LC materials-combine colloidal quantum dots (QDs) and cholesteric liquid crystal networks (CLCNs) to produce extended wide color palettes of both photoluminescence and Bragg reflection (Figure 1b). 2C printing is defined as an inkjet printing technology to create full-color, high-resolution, and geminate patterns carrying crosstalk-free images with two colors of different mechanisms, e.g., fluorescent *Dragon* and reflective *Phoenix* (Figure 1c,d; Video S2, Supporting Information). It should be emphasized that 2C printing, which prints QD and LC inks into the CLCNs in sequence, enables the construction and precise patterning of the fluorescent LC nanocomposites at the same time (Figure 1e). Moreover, we demonstrate the decoupled encryption of multiple codes in geminate security labels by 2C printing to show the potential of our fluorescent LC nanocomposites as carriers in anti-counterfeiting technologies.

2. Results and Discussion

The skin-inspired geminate patterns were designed according to two criteria: 1) the gamut of both photoluminescence and Bragg reflection must be wide, and 2) the fluorescent and reflective images must be high-resolution. The first requirement is

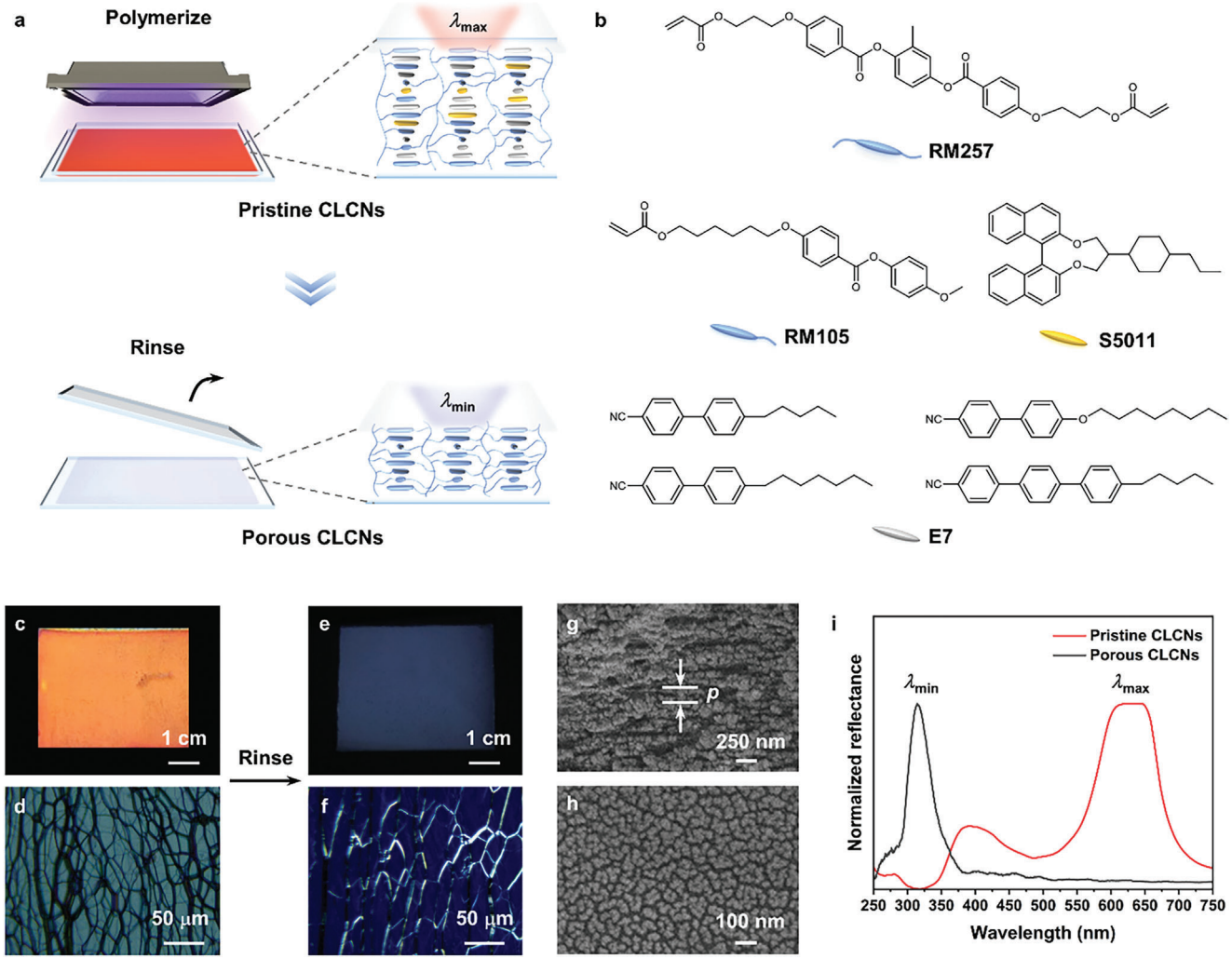

Figure 2. a) Schematic illustration to show the fabrication process of the porous CLCNs. After the complete removal of the CLC solvent in the pristine CLCNs, the polymer networks shrink along the thickness direction, leading to the blueshift of the reflection wavelength from λ_{max} to λ_{min}. b) Chemical structures of the crosslinker RM257, monomer RM105, chiral dopant S5011, and nematic LC E7. The RM 257 and RM105 are polymerized to form the CLCNs with the aid of the CLC solvent consisting of S5011 and E7, which are completely removed by rinsing. c) A photograph of the red pristine CLCNs confined in a 50 μm thick LC cell. d) A polarized optical microscopy (POM) image to show the oily streak textures of the pristine CLCNs. e) A photograph of the transparent porous CLCNs. The thickness of the CLCNs is 21 μm. f) A POM image to show the oily streak textures of the porous CLCNs. g,h) SEM images of the porous CLCNs to show morphologies of cross-section g) and surface h). The pitch length was marked with white lines. i) Reflection spectra of the pristine (red) and porous (black) CLCNs showing the λ_{max} at 630 nm and the λ_{min} at 313 nm, respectively.

satisfied by designing the novel fluorescent LC nanocomposites, whose planarly aligned helical superstructures are stabilized by the polymer networks. The QD nanoparticles are embedded in the CLCNs to exhibit bright multicolor luminescence based on the Grassmann color mixing law. Correspondingly, the LC eutectic mixtures swell the CLCNs to alter the pitch lengths of the helical superstructures and tune the structural colors across the visible spectrum based on Bragg's law. To satisfy the second criterion, an ideal patterning method is the reliable drop-on-demand inkjet printing technology, which handles minute amounts of ink processed into defined droplets on every pixel.[37–39] The prerequisite for creating geminate patterns is the printing-directed decoupled coloration scheme, where the fluorescent and structural colors should be independently tuned in an accurate manner. From these principles, 2C printing is established to sequentially print QD and LC inks into the CLCNs, creating full-color, high-resolution, and geminate patterns with distinct fluorescent and reflective images.

In this "paper-ink" system, the CLCNs serving as printable photonic paper are the key elements, which should provide porous structures to embed QDs and be swelled by the LC inks. The porous CLCNs were fabricated in two steps: 1) polymerization of the homogeneous CLC mixtures to form the networks of planarly aligned helical superstructures with the maximum reflection wavelength (λ_{max}), and 2) removal of the non-polymerizable CLC solvent to obtain the porous CLCNs with the minimum reflection wavelength (λ_{min}; **Figure 2a**; the details are described in Methods). Figure 2b shows the chemical

composition of the CLC homogenous mixtures. The helical superstructures are induced by the chiral dopant S5011 with high helical twisting power (120 μm^{-1}, wt.%; Figure S1, Supporting Information) and fixed by the photopolymerization of the crosslinker RM257 and monomer RM105 in the presence of the CLC solvent (S5011 in nematic LC E7). After the complete removal of the CLC solvent (testified by FT-IR spectra in Figure S2, Supporting Information), the pristine CLCNs changed from red to transparent (near ultraviolet) due to the decrease of the pitch length, since the networks collapsed and shrank along the thickness direction (Figure 2c,e). Both the red pristine CLCNs and transparent porous CLCNs possessed typical oily streak textures that confirmed the formation of planarly aligned helical superstructures (Figure 2d,f). Furthermore, the cross-sectional scanning electron microscopy (SEM) image of the porous CLCNs directly shows periodically lamellar structures (Figure 2g). Thus, the CLCNs are qualified as printable photonic paper because the removal of the CLC solvent generates porous structures (≈20 nm) inside and at the surface (Figure 2g,h), which offer space for printing QD and LC inks.[40,41] As the reflectance spectra shown in Figure 2i, the central reflection wavelength of the helical superstructures shifted from λ_{max} at 630 nm to λ_{min} at 313 nm, ensuring a wide tuning range of the structural colors across the visible spectrum. Moreover, owing to the planarly aligned helical superstructures, the CLCNs as 1D photonic crystal architectures cause angle-dependent reflection upon white light irradiation (Figure S3, Supporting Information).

Core–shell CdSe/ZnS QDs were chosen as the fluorescent nanoparticles due to the small diameters (< 20 nm porous structures), size-dependent emission attributed to quantum confinement effect,[42–45] facile generation of multicolor luminescence (**Figure 3**a), high quantum yield efficiency, and solution processibility. The QDs with different average sizes (Figure S4, Supporting Information) exhibit symmetric RGB emission peaks at 628, 517, 460 nm with 25, 28, 20 nm full width at half-maximum (FWHM) values, respectively (Figure 3b). We demonstrated secondary colors (yellow, cyan, and magenta) and even white light emission simply by mixing the RGB QDs (Figure 3a), whose corresponding photoluminescence spectra showed independent RGB emission peaks with acceptable photo-stability as expected (Figure S5 and S6, Supporting Information). It is noted that the color space enclosed in a triangle with three primary colors at the vertices completely covers more than sRGB space in CIE coordinate (Figure 3c), indicating a wide gamut and high purity of each primary color (narrow FWHM).

The inks should possess suitable viscosity and optimized wettability to create high-resolution patterns. The former contributes to the reliable ejection of bursts of microdroplets, while the latter facilitates rapid spreading out on the surface and in situ diffusion. To this end, the QDs were evenly dispersed into a volatile acrylic resin solution to meet the requirements in the aspects of viscosity (η < 15 cps) and wettability as printing ink, which showed a wetting state with contact angles less than 10° (Figure S7, Supporting Information). By adjusting the driving sine waveform and printing frequency, uniform 20 pL droplets of the QD inks were consecutively ejected from the printhead and each droplet generated a 100-µm-diameter color spot on the CLCNs that were heated to 60 °C. During this procedure, the ink droplets first spread out on the surface and then immediately swell the polymer networks by diffusion. Eventually, after evaporation of the acrylic resin solution at 60 °C for 30 min, the QDs are embedded into the porous structures of the CLCNs, the deswelling of which leads to the constant pitch length of the helical superstructures.

Sequentially printing the RGB QD inks at 80 µm spot-to-spot spacing created colorful fluorescent images, e.g., *Plum blossom* and *Orchid*, with a resolution as high as ca. 300 dots per inch (DPI) (Figure 3d,e). Importantly, the measurement of the surface height shows no increase in the thickness of the CLCNs (Figure 3f), which indirectly signifies the constant pitch length of the helical superstructures after the introduction of the QDs (Figure S8, Supporting Information). Furthermore, all the reflection spectra exhibit peaks at 313 nm which is the same as the λ_{min}, testifying that the pitch length of the printed CLCNs is consistent with that of the porous CLCNs before printing (Figure 3g). This phenomenon satisfies the prerequisite for decoupled coloration of photoluminescence and Bragg reflection, and is ascribed to two factors: 1) the porous structures of the CLCNs provide reserved room for the introduction of the QDs, which has no effect on the pitch length of the planarly aligned helical superstructures; 2) because of the high quantum yield efficiencies of the QDs (φ > 50%), printing extraordinarily tiny amounts of the QDs (calculated by nanogram) is adequate to produce bright visible fluorescent images.

The LC inks (nematic LC E7) were refilled by inkjet printing to swell the CLCNs, causing an increase in the local surface height and redshift of the structural colors. The printhead was heated to the nematic-to-isotropic phase transition temperature at 60 °C to reduce the viscosity of the LC inks (13.7 cps; Figure S9, Supporting Information). In addition, the CLCNs were also heated to 60 °C to enhance the diffusion rate and ensure the uniform distribution of the LC inks. Similarly, high-contrast reflective images, e.g., *Bamboo* and *Chrysanthemum*, with ca. 300 DPI resolution were created by printing the LC inks with different layers (Figure 3h,i; Figure S10, Supporting Information). The structural colors ranging from blue to red are determined by the layer number of the LC inks that induce the increase in the surface height profile owing to an expansion of the CLCNs along the thickness direction (Figure 3j; Figure S11, Supporting Information). Therefore, as the number of print layers increases to 10, the experimental reflection wavelengths of the CLCNs redshift from λ_{min} at 313 to 590 nm, which are in accordance with the theoretical values calculated by the increased thickness of the CLCNs (Figure 3k; Table S1, Supporting Information).

It is noted that both lateral diffusion and transverse diffusion occur when an LC droplet swells the CLCNs (**Figure 4**a). In this scenario, the anisotropy of the LCs and self-organized layer-by-layer helical fashion typically give rise to a preferred lateral diffusion.[46,47] Therefore, if one LC droplet (ca. 20 pL) is completely absorbed by the CLCNs, the surface height will increase by 2.4 µm in theory on the basis of volume conversion from a sphere (R_1 = 16.5 µm) to a cylinder (R_2 = 50 µm) (Figure 4b). Experimentally, the increased surface height (Δh) of each layer matches well at the beginning and however gradually deviates from the theoretical value as the printing layer increases; meanwhile, the widths of the lines increase. These results indicate that transverse diffusion is inevitable (Table S1, Supporting Information).

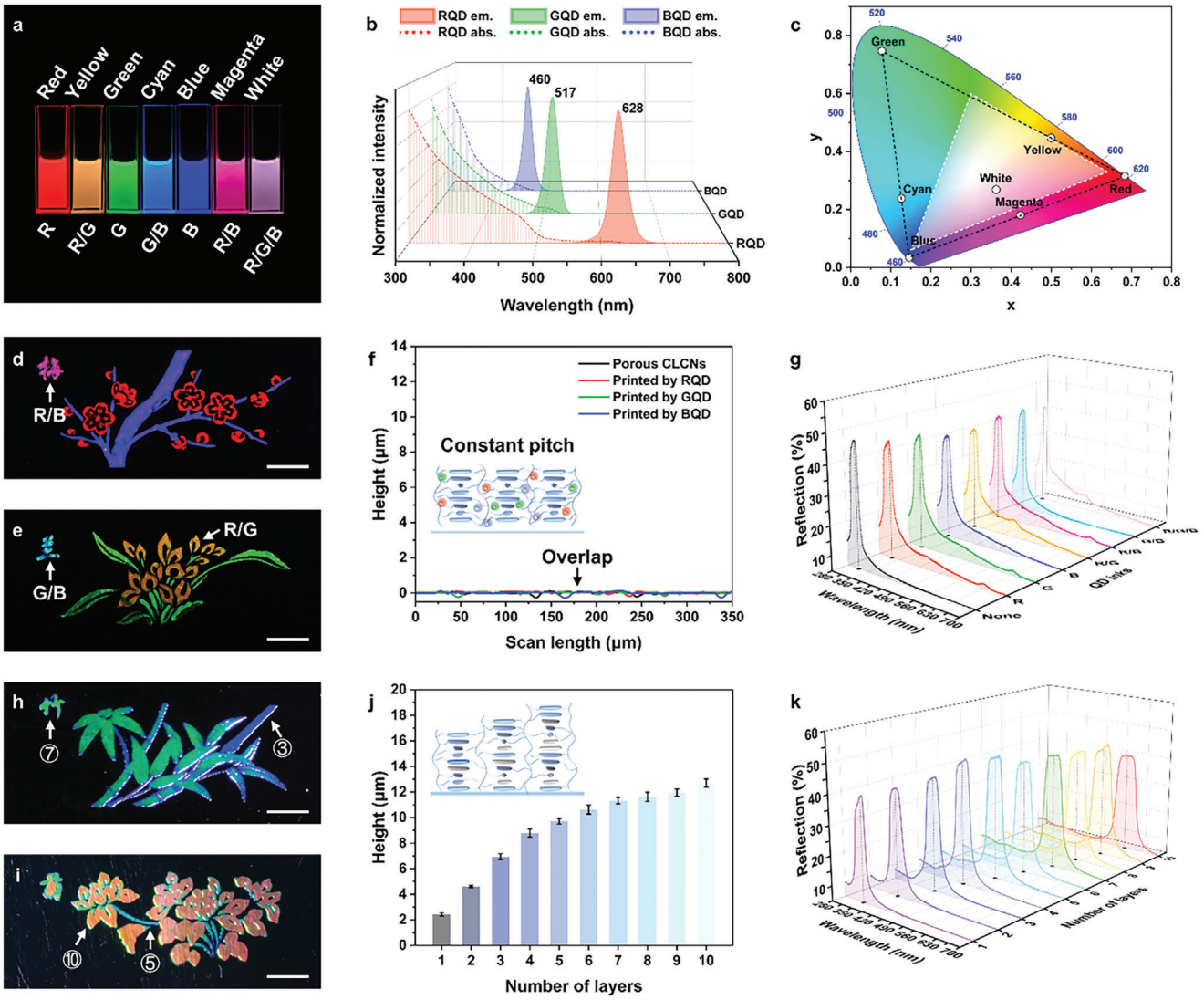

Figure 3. a) A photograph of the diluted QD inks in toluene to show the primary colors (red, green, blue), secondary colors (yellow, cyan, magenta), and white color upon UV excitation. The yellow, cyan, and magenta colors are obtained by mixing R/G, G/B, and R/B QD inks in toluene in equal proportions, respectively. The white color is obtained by mixing R/G/B diluted QD inks in toluene in equal proportions. $c_R = 2.2 \times 10^{-6}$ g mL^{-1}, $c_G = 6.0 \times 10^{-6}$ g mL^{-1}, and $c_B = 6.0 \times 10^{-6}$ g mL^{-1}. b) Photoluminescence spectra and absorption spectra of the diluted RQD, GQD, and BQD inks in toluene. c) CIE chromaticity coordinates of the QD inks with different fluorescent colors. Red (0.68, 0.31), Green (0.078, 0.75), Blue (0.15, 0.035). The regions enclosed by black and white dashed lines present the color space in this work and sRGB space, respectively. d,e) Photographs of the CLCNs printed by the QD inks to show fluorescent images, *Plum blossom* d) and *Orchid* e). R/G, G/B, and R/B denote the QD inks used to generate yellow, cyan, and magenta colors, respectively. Scale bar, 5 mm. f) A plot to show the surface height of the porous CLCNs and the CLCNs printed by the QD inks. Inset, schematic illustration to show the constant pitch lengths of the CLCNs printed by the QD inks. g) Reflection spectra of the porous CLCNs (None) and the CLCNs printed by the QD inks. All the printed CLCNs exhibit the reflection wavelength at 313 nm, which is the same as the λ_{min} (313 nm) of the porous CLCNs. h,i) Photographs of the CLCNs printed by the LC inks to show reflective images, *Bamboo* h) and *Chrysanthemum* i). ③, ⑤, ⑦, and ⑩ denote the layer number of the LC inks. Scale bar, 5 mm. j) A plot to show the surface height of the CLCNs printed by the LC inks with different layers. Inset, schematic illustration to show the tunable pitch lengths of the CLCNs printed by the LC inks with different layers. k) Reflection spectra of the CLCNs printed by the LC inks with different layers. The reflection wavelength gradually redshifts from 313 to 590 nm as the number of print layers increases.

To gain further insight into 2C printing, the creation procedure of the geminate pattern with two different *Chinese opera mask* images was investigated in detail (Figure S12, Supporting Information; the details are described in Methods). Both the fluorescent and reflective images are translated to print files containing several bitmaps of pixel arrays that illustrate the print paths of required inks and the number of print layers (Figure 4c,d). First, each RGB QD ink is printed once with a 30 min interval for complete evaporation of the ink solution to create the fluorescent *Chinese opera mask* image. The stepwise printing of the LC inks into the CLCNs with a 30 min interval for diffusion creates the reflective image, whose layout is entirely different from that of the

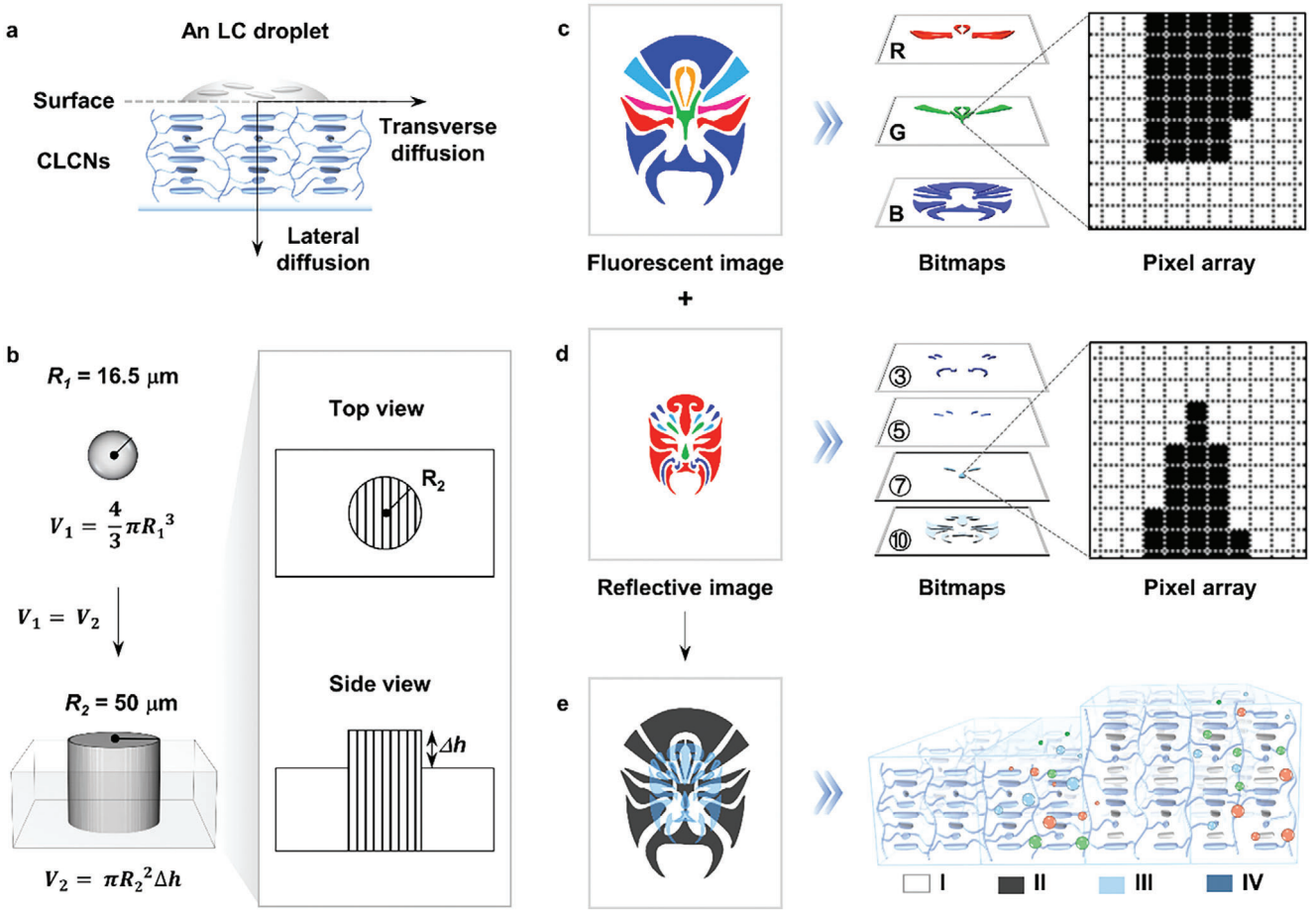

Figure 4. a) Schematic illustration to show lateral diffusion and transverse diffusion of an LC droplet on the surface of the CLCNs. b) Theoretical model to show the variation in surface height of the CLCNs printed by one LC droplet. The increased surface height (Δh) is calculated as 2.4 μm. c,d) Schematic illustration to show the translation of the fluorescent image c) and reflective image d) to print files. The fluorescent image is translated to bitmaps that illustrate the colors of the QD inks. The reflective image is translated to bitmaps that illustrate the printing layers of the LC inks. All the bitmaps are divided into a pixel array and the expanded view of the partial pixel array (10 × 10) in the print files is shown as an example. The black squares present the areas (pixels) that should be printed by a 20 pL droplet of the QD or LC inks. The size of the fluorescent *Chinese opera mask* is 214 × 290 pixels. The size of the reflective *Chinese opera mask* is 158 × 214 pixels. The spot-to-spot spacing is set as 80 μm. e) Schematic illustration to show four areas distributed over the CLCNs. I, original area; II, fluorescent area; III, reflective area; IV, geminate area.

fluorescent image. Consequently, four areas are distributed over the CLCNs, including the original areas, fluorescent areas, reflective areas, and geminate areas (Figure 4e). These results manifest that our 2C printing simultaneously enables the construction and patterning of the fluorescent LC nanocomposites.

Both wide gamuts of photoluminescence and Bragg reflection in 2C printing technology determine the best possible color fidelity of the printed geminate images. An in situ color palette was created by selectively printing QD and LC inks into a square matrix (**Figure 5**a), demonstrating the unlimited orthogonal combination of fluorescent and structural colors in theory (Figure 5b,c). The squares in the row exhibit the same luminescence but diverse structural colors since the pigment colors of the embedded QDs are concealed by the structural colors from the helical superstructures.[28] The squares in the column exhibit the same structural colors but multicolor luminescence. Compared to the low-molar-mass LC,[29–32] the CLCNs acting as high-tolerance polymer solutions improve the compatibility with various fluorescent materials, which are no longer limited to the AIE property, therefore greatly widening the fluorescent color palette. Equally crucial is the controllable pitch length that remains constant after the introduction of the QDs and precisely increases by swelling of the LC inks with different layers. Most importantly, the squares in the first column are all transparent (λ_{min} at 313 nm) upon white light irradiation and become visible upon UV excitation, which provides indispensable "black" reflection (area II in Figure 4e) to create geminate patterns with entirely different profiles.

As a proof of concept, we create a geminate security label by 2C printing technology to carry multiple codes with crosstalk-free information (Figure 5d), demonstrating advanced encryption with high security, good concealment, large storage capacity, and simple identification. The security level is enhanced by rich hues in two color palettes as well as angle-dependent structural colors. The planarly aligned helical superstructures as 1D photonic crystal architectures cause the angle-dependent reflection upon

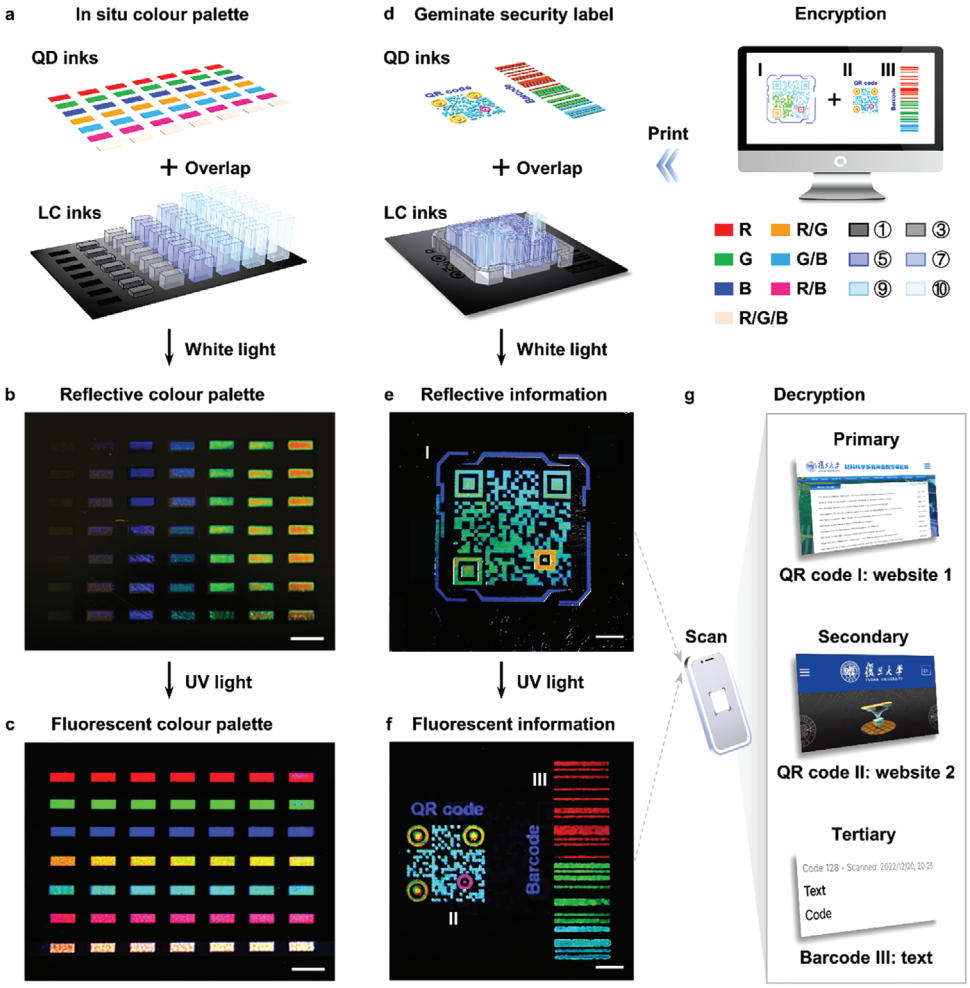

Figure 5. a) Schematic illustration to show an in situ color palette created by 2C printing technology. b,c) Photographs of the in situ color palette to show a wide gamut combining both structural colors b) and fluorescent colors c). Scale bar, 5 mm. d) Schematic illustration to show information encryption of a geminate security label. The fluorescent and reflective images are analyzed in the computer to export a blueprint that indicates the required inks and print paths. R, G, and B denote the fluorescent colors of the QD inks; ①, ③, ⑤, ⑦, ⑨, and ⑩ denote the layer number of the LC inks. e,f) Photographs of the geminate security label to show the triple information of color coding, including reflective QR code I e), fluorescent QR code II and barcode III f). Scale bar, 5 mm. g) Decryption of the geminate security label by a smartphone to show the primary (website 1), secondary (website 2), and tertiary (text) information.

white light irradiation, while the omnidirectional emission of the QDs determines the angle-independent fluorescence upon UV excitation (Figure S13, Supporting Information). The decoupled coloration of photoluminescence and Bragg reflection contributes to that arbitrary fluorescent information can be completely concealed behind custom reflective information (Figure 5e,f). The information capacity of the label is enlarged by high-definition 2C printing technology that controls the distribution of two colors down to the microscale at the same time. Therefore, multiple codes were integrated into one geminate security label (Figure 5g), including the colorful reflective QR code (website of our lab), fluorescent QR code (website of Fudan University), and barcode (text of "code"). Following the above fundamentals, all the programmed crosstalk-free information with stable reflective and fluorescent codes (Figure S14, Supporting Information) are machine-readable mediums accessible to the average person (Video S3, Supporting Information).

3. Conclusion

In summary, inspired by animal skins we created full-color, high-resolution geminate patterns. Toward this end, a 2C printing technology was proposed to construct novel fluorescent LC nanocomposites with orthogonally tunable photoluminescence and Bragg reflection. The nanocomposites were fabricated by embedding QDs and LCs into the porous CLCNs for obtaining wide gamuts of both structural and fluorescent colors. Especially, the two colors were decoupled because the nanoscale QDs have no impact on the pitch lengths of the fixed helical superstructures in CLCNs. The concept of coating the fluorescent materials with structural colors from ordered periodic architectures opens great opportunities to design new optical materials that produce both chemical and physical colors. Taking advantage of the drop-on-demand 2C printing technology to programmatically introduce QD and LC inks into the CLCNs, high-resolution fluorescent and

reflective images are created. Such patterning method that provides two different types of extended color gamut could be generalized to diverse photonic crystals, such as opal/inverse opal structures constructed by colloidal crystals, and lamellar structures assembled by block polymers. As proof-of-concept demonstrations, the security label has been designed to encrypt multiple fluorescent codes, such as QR codes and barcodes, behind reflective codes with entirely distinct information to deter counterfeits. The ability of the geminate labels to enhance the anti-counterfeiting level is anticipated to be further updated by either the pigment colors in the skins or stimuli-responsive colors to show diverse optical modes.

4. Experimental Section

Materials: All chemical reagents were purchased from Adamas-beta and were used as supplied without further purification. The nematic LC E7 (n = 1.747, T_c = 60 °C) was purchased from Nanjing Murun Advanced Material Co., Ltd. The crosslinker RM257 and monomer RM105 were purchased from Shijiazhuang Sdyano Fine Chemical Co., Ltd. The chiral dopant S5011 was purchased from Jiangsu Hecheng Display Technology Co., Ltd. The polyimide (PI) prepolymers for the alignment layer were purchased from Kelide Optoelectronic Materials Co., Ltd. The RQD inks (c = 2 wt.%, ρ = 1.19 g mL^{-1}, η = 9.4 cps, φ = 52.2%), GQD inks (c = 5 wt.%, ρ = 1.20 g mL^{-1}, η = 11.5 cps, φ = 57.1%), and BQD inks (c = 5 wt.%, ρ = 1.19 g mL^{-1}, η = 9.5 cps, φ = 65.0%) were purchased from Guangdong Pujiafu Photoelectric Technology Co., Ltd. The spacers (polyethylene terephthalate films, 50 µm) were purchased from Suzhou Dongxuan Plastic Products Co., Ltd. The wedge cells (KCRK-07) were purchased from Beijing Bayi Space Computer Co., Ltd.

Fabrication of the LC Cells: First, all glass substrates (5 cm × 6 cm) were cleaned by sonication in ethanol for 3 h and treated with oxygen plasma for 300 s to activate the glass surfaces. Second, the bottom glass substrates of the LC cells were spin-coated (3000 rpm, 40 s) with 1 vol% 3-(trimethoxysilyl)propyl methacrylate in water-isopropanol solution (1:1 volume ratio), followed by curing at 100 °C for 20 min. The methacrylate-functionalized coating was covalently bonded to the CLCNs to fix the film on the glass. The upper glass substrates of the LC cells were spin-coated (3000 rpm, 40 s) with PI prepolymers that were subsequently cured by two-step imidization at 80 °C for 1 h and 240 °C for 2 h. The PI-coated glass substrates were then mechanically rubbed with a rayon velvet cloth by a rubbing machine (HOLMARC, HO-IAD-BTR-02), generating the alignment layer parallel to the rubbing direction. Last, stick the 50 µm spacers on either side of the bottom glass substrates, which were bound with the upper glass substrates to fabricate the LC cells by UV-curable adhesive.

Fabrication of the Printable CLCNs: Step I: the homogeneous CLC mixtures consisting of 20 wt.% RM257, 31 wt.% RM105, 2.1 wt.% S5011, 45.9 wt.% E7, and 1 wt.% Irgacure 651 were filled into the homemade LC cells by capillary force on a heating stage at 50 °C below the cholesteric-to-nematic phase transition temperature (59 °C; Figure S15, Supporting Information). The CLC mixtures formed planarly aligned helical superstructures and were fixed by photopolymerization upon exposure to UV light (2 mW cm^{-2}, 20 min) to obtain red pristine CLCNs (polymer networks with the CLC solvent). Step II: peel off the upper PI-coated glass substrates and immerse the pristine CLCNs in tetrahydrofuran (THF) for 1 h to remove the unreacted RM257, RM105, and non-polymerizable CLC solvent (S5011 in E7). The acrylate-based CLCNs were attached to the bottom glass substrates modified by a methacrylate-based layer. After evaporation of THF in a vacuum oven at 50 °C, the transparent porous CLCNs (neat polymer networks) were obtained and qualified as printable photonic paper.

Fabrication of the Fluorescent and Reflective Images by Inkjet Printing: The CLCNs were heated to 60 °C before printing to enhance the diffusion rate of both the QD and LC inks. The nozzle (MJ-AL-01-40-8MX) with a 40 µm-diameter orifice was used to eject discrete bursts of ink droplets. The volume for each ink droplet was controlled as 20 pL and the spot-to-spot spacing was set as 80 µm. Printing of the QD inks: a driving sine waveform (40 V dwell voltage, 16 µs nominal period) was implemented to print the QD inks into the CLCNs at a printing frequency set to 300 Hz. The fluorescent images were fabricated by printing RQD, GQD, and BQD inks in sequence, followed by evaporation of the solvent at 60 °C for 30 min to maintain the original pitch length. The total time for creating a fluorescent image is ≈30 min. Printing of the LC inks: the nozzle was filled with the nematic LC E7 and heated to 60 °C for 1.5 h to reduce the viscosity of the E7 (13.7 cps). A driving sine waveform (60 V dwell voltage, 10 µs nominal period) was implemented to print the LC E7 into the CLCNs at a printing frequency set to 400 Hz. The reflective images were fabricated by printing the LC E7 with different layers. The total time for creating a reflective image is ≈2–3 h.

Measurements: The textures of the CLCNs and the disclination lines of the CLC mixtures were observed by using a polarized optical microscope (OPTEC BK-POL). Reflection spectra of the CLCNs were recorded by using a reflection spectrometer (Ideaoptics Instruments PG2000-Pro-EX, 200–1100 nm). The morphologies of the CLCNs inside and at the surface were observed by using field emission scanning electron spectroscopy (Zeiss Gemini 300). The phase transition temperature of the CLC mixtures was measured by using a differential scanning calorimeter (TA instrument Q2000) at a scanning rate of 10 °C min^{-1}. FT-IR spectra were measured by using an FT-IR spectrometer (Nicolet NEXUS 470) at a resolution of 4 cm^{-1}. UV–vis spectra of the QD inks were measured by using a UV-vis spectrometer (PerkinElmer Lambda 650, 200–800 nm) at a resolution of 2 nm. Photoluminescence spectra of the QD inks were measured by using a spectrofluorometer (Shimadzu RF6000) at intervals of 1 nm. Photobleaching resistance of the QD inks was collected by using a spectrofluorometer (Shimadzu RF6000) upon 365 nm UV excitation for 60 min. The morphologies of the QDs were observed by using a transmission electron microscope (JEOL JEMF200). The mean diameters of the QDs were estimated by using time-resolved dynamic light scattering (Malvern ZS90). Inkjet printing was carried out by using a printer (Microfab Jetlab4) equipped with a 40 µm-diameter nozzle. The height of the CLCNs printed by the inks with different layers was measured by using a stylus profilometer (Bruker Dktak XT). 365 nm UV light was generated by using a light source (Omron ZUV-H30MC) with a controller (ZUV-C30H). Photographs and videos were recorded using a digital camera (Canon EOS 70D).

Supporting Information

Supporting Information is available from the Wiley Online Library or from the author.

Acknowledgements

This work was financially supported by the National Natural Science Foundation of China (52173110, 51721002), National Key R&D Program of China (2017YFA0701302), Natural Science Foundation of Shanghai (21ZR1405900), and Shanghai Rising-Star Program (22QA1401200).

Conflict of Interest

The authors declare no conflict of interest.

Data Availability Statement

The data that support the findings of this study are available from the corresponding author upon reasonable request.

Keywords

cholesteric liquid crystal networks, inkjet printing, photoluminescence, photonic crystals, structural colors

Received: October 11, 2023
Revised: December 5, 2023
Published online:

[1] A. Orteu, C. D. Jiggins, *Nat. Rev. Genet.* **2020**, *21*, 461.
[2] T. L. Williams, S. L. Senft, J. Yeo, F. J. Martín-Martínez, A. M. Kuzirian, C. A. Martin, C. W. Dibona, C.-T. Chen, S. R. Dinneen, H. T. Nguyen, C. M. Gomes, J. J. C. Rosenthal, M. D. Macmanes, F. Chu, M. J. Buehler, R. T. Hanlon, L. F. Deravi, *Nat. Commun.* **2019**, *10*, 1004.
[3] D. G. Stavenga, H. L. Leertouwer, B. D. Wilts, *J Exp Biol* **2014**, *217*, 2171.
[4] S. V. Saenko, J. Teyssier, D. Van Der Marel, M. C. Milinkovitch, *BMC Biol.* **2013**, *11*, 105.
[5] D. Nepal, S. Kang, K. M. Adstedt, K. Kanhaiya, M. R. Bockstaller, L. C. Brinson, M. J. Buehler, P. V. Coveney, K. Dayal, J. A. El-Awady, L. C. Henderson, D. L. Kaplan, S. Keten, N. A. Kotov, G. C. Schatz, S. Vignolini, F. Vollrath, Y. Wang, B. I. Yakobson, V. V. Tsukruk, H. Heinz, *Nat. Mater.* **2023**, *22*, 18.
[6] Y. Zhang, P. Han, H. Zhou, N. Wu, Y. Wei, X. Yao, J. Zhou, Y. Song, *Adv. Funct. Mater.* **2018**, *28*, 1802585.
[7] M. Sakai, T. Seki, Y. Takeoka, *Small* **2018**, *14*, 1800817.
[8] I. Kim, J. Jang, G. Kim, J. Lee, T. Badloe, J. Mun, J. Rho, *Nat. Commun.* **2021**, *12*, 3614.
[9] J. Yan, G. Pan, W. Lin, Z. Tang, J. Zhang, J. Li, W. Li, X. Lin, H. Luo, G. Yi, *Chem. Eng. J.* **2023**, *451*, 138922.
[10] R. Arppe, T. J. Sørensen, *Nat. Rev. Chem.* **2017**, *1*, 0031.
[11] P. Kumar, S. Singh, B. K. Gupta, *Nanoscale* **2016**, *8*, 14297.
[12] A. Abdollahi, H. Roghani-Mamaqani, B. Razavi, M. Salami-Kalajahi, *ACS Nano* **2020**, *14*, 14417.
[13] Y. Sun, X. Le, S. Zhou, T. Chen, *Adv. Mater.* **2022**, *34*, 2201262.
[14] W. Tian, J. Zhang, J. Yu, J. Wu, J. Zhang, J. He, F. Wang, *Adv. Funct. Mater.* **2018**, *28*, 1703548.
[15] X. Chen, H. K. Bisoyi, X.-F. Chen, X.-M. Chen, S. Zhang, Y. Tang, G. Zhu, H. Yang, Q. Li, *Matter* **2022**, *5*, 3883.
[16] Q. Wang, B. Lin, M. Chen, C. Zhao, H. Tian, D.-H. Qu, *Nat. Commun.* **2022**, *13*, 4185.
[17] X. Yang, C. Valenzuela, X. Zhang, Y. Chen, Y. Yang, L. Wang, W. Feng, *Matter* **2023**, *6*, 1278.
[18] S.-U. Kim, Y.-J. Lee, J. Liu, D. S. Kim, H. Wang, S. Yang, *Nat. Mater.* **2022**, *21*, 41.
[19] L. Qin, W. Gu, J. Wei, Y. Yu, *Adv. Mater.* **2018**, *30*, 1704941.
[20] J. A. H. P. Sol, L. G. Smits, A. P. H. J. Schenning, M. G. Debije, *Adv. Funct. Mater.* **2022**, *32*, 2201766.
[21] X. Zhang, Y. Yang, P. Xue, C. Valenzuela, Y. Chen, X. Yang, L. Wang, W. Feng, *Angew. Chem., Int. Ed.* **2022**, *61*, e202211030.
[22] J. Ma, Y. Yang, C. Valenzuela, X. Zhang, L. Wang, W. Feng, *Angew. Chem., Int. Ed.* **2021**, *61*, e202116219.
[23] X. Liu, L. Qin, Y. Yu, *Acta Phys.-Chim. Sin.* **2024**, *40*, 2305018.
[24] R. Chen, D. Feng, G. Chen, X. Chen, W. Hong, *Adv. Funct. Mater.* **2021**, *31*, 2009916.
[25] R. Lan, J. Bao, Z. Li, Z. Wang, C. Song, C. Shen, R. Huang, J. Sun, Q. Wang, L. Zhang, H. Yang, *Angew. Chem., Int. Ed.* **2022**, *61*, e202213915.
[26] Z. Zheng, H. Hu, Z. Zhang, B. Liu, M. Li, D.-H. Qu, H. Tian, W.-H. Zhu, B. L. Feringa, *Nat. Photonics* **2022**, *16*, 226.
[27] Y. Zhao, X. Zhao, M.-D. Li, Z. Li, H. Peng, X. Xie, *Angew. Chem., Int. Ed.* **2020**, *59*, 10066.
[28] L. Qin, X. Liu, K. He, G. Yu, H. Yuan, M. Xu, F. Li, Y. Yu, *Nat. Commun.* **2021**, *12*, 699.
[29] S. Lin, K. G. Gutierrez-Cuevas, X. Zhang, J. Guo, Q. Li, *Adv. Funct. Mater.* **2021**, *31*, 2007957.
[30] H. K. Bisoyi, Q. Li, *Chem. Rev.* **2022**, *122*, 4887.
[31] Z. Chi, X. Zhang, B. Xu, X. Zhou, C. Ma, Y. Zhang, S. Liu, J. Xu, *Chem. Soc. Rev.* **2012**, *41*, 3878.
[32] J. Voskuhl, M. Giese, *Aggregate* **2021**, *3*, 124.
[33] W. Z. Yuan, Z.-Q. Yu, P. Lu, C. Deng, J. W. Y. Lam, Z. Wang, E.-Q. Chen, Y. Ma, B. Z. Tang, *J. Mater. Chem.* **2012**, *22*, 3323.
[34] J. W. Park, S. Nagano, S.-J. Yoon, T. Dohi, J. Seo, T. Seki, S. Y. Park, *Adv. Mater.* **2014**, *26*, 1354.
[35] S.-J. Yook, J. H. Kim, K. S. Kim, J. W. Chung, B. Heinrich, F. Mathevet, P. Kim, B. Donnio, A.-J. Attias, D. Kim, S. Y. Park, *Adv. Funct. Mater.* **2012**, *22*, 61.
[36] J. Li, H. K. Bisoyi, J. Tian, J. Guo, Q. Li, *Adv. Mater.* **2019**, *31*, 1807751.
[37] L. Wu, Z. Dong, F. Li, H. Zhou, Y. Song, *Adv. Opt. Mater.* **2016**, *4*, 1915.
[38] W. Ren, G. Lin, C. Clarke, J. Zhou, D. Jin, *Adv. Mater.* **2020**, *32*, 1901430.
[39] D. Li, J. Wang, M. Li, G. Xie, B. Guo, L. Mu, H. Li, J. Wang, H.-L. Yip, J. Peng, *Adv. Mater. Technol.* **2020**, *5*, 2000099.
[40] Y. Zhan, D. J. Broer, D. Liu, *Adv. Mater.* **2023**, *35*, 2211143.
[41] A. P. H. J. Schenning, D. J. Broer, *Adv. Funct. Mater.* **2018**, *28*, 1705942.
[42] F. P. García De Arquer, D. V. Talapin, V. I. Klimov, Y. Arakawa, M. Bayer, E. H. Sargent, *Science* **2021**, *373*, aaz8541.
[43] Y. Shu, X. Lin, H. Qin, Z. Hu, Y. Jin, X. Peng, *Angew. Chem., Int. Ed.* **2020**, *59*, 22312.
[44] W. R. Algar, M. Massey, K. Rees, R. Higgins, K. D. Krause, G. H. Darwish, W. J. Peveler, Z. Xiao, H.-Y. Tsai, R. Gupta, K. Lix, M. V. Tran, H. Kim, *Chem. Rev.* **2021**, *121*, 9243.
[45] M. Yu, M. H. Saeed, S. Zhang, H. Wei, Y. Gao, C. Zou, L. Zhang, H. Yang, *Adv. Funct. Mater.* **2022**, *32*, 2109472.
[46] M. Moirangthem, A. F. Scheers, A. P. H. J. Schenning, *Chem. Commun.* **2018**, *54*, 4425.
[47] M. Moirangthem, A. P. H. J. Schenning, *ACS Appl. Mater. Interfaces* **2018**, *10*, 4168.